ADVANCED MATERIALS
www.advmat.de

Visualizing the Internal Nanocrystallinity of Calcite Due to Nonclassical Crystallization by 3D Coherent X-Ray Diffraction Imaging

Ana F. Suzana, Sang Soo Lee, Irene Calvo-Almazán, Wonsuk Cha, Ross Harder, and Paul Fenter*

The internal crystallinity of calcite is investigated for samples synthesized using two approaches: precipitation from solution and the ammonium carbonate diffusion method. Scanning electron microscopy (SEM) analyses reveal that the calcite products precipitated using both approaches have a well-defined rhombohedron shape, consistent with the euhedral crystal habit of the mineral. The internal structure of these calcite crystals is characterized using Bragg coherent diffraction imaging (BCDI) to determine the 3D electron density and the atomic displacement field. BCDI reconstructions for crystals synthesized using the ammonium carbonate diffusion approach have the expected euhedral shape, with internal strain fields and few internal defects. In contrast, the crystals synthesized by precipitation from solution have very complex external shapes and defective internal structures, presenting null electron density regions and pronounced displacement field distributions. These heterogeneities are interpreted as multiple crystalline domains, created by a nonclassical crystallization mechanism, where smaller nanoparticles coalescence into the final euhedral particles. The combined use of SEM, X-ray diffraction (XRD), and BCDI allows for structurally differentiating calcite crystals grown with different approaches, opening new opportunities to understand how grain boundaries and internal defects alter calcite reactivity.

1. Introduction

Calcium carbonate ($CaCO_3$) is one of the most abundant minerals, occurring mostly in the form of limestone and chalk. $CaCO_3$ is present in three different anhydrous polymorphs under ambient conditions: aragonite, vaterite, and calcite.[1] Besides these phases, amorphous calcium carbonate (ACC, hydrated and dehydrated), and two hydrated crystalline phases (hexahydrate ikaite and monohydrocalcite) are also known.[1,2] The most thermodynamically stable phase, calcite, has rhombohedral shape while metastable aragonite and vaterite are acicular and spherical, respectively.[3] The formation of these polymorphs is dependent on parameters such as temperature and pH, as well as the saturation indices of the solids, where the latter has been pointed to be the main controlling factor.[4] The saturation index with respect to each calcium carbonate polymorph is defined commonly as the logarithmic ratio of the ion activity product to the solubility product of that solid phase. Additives have been previously used to control the formation of specific calcium carbonate phases.[5,6] The synthesis of calcium carbonate is an important topic as it involves the transformation of carbon dioxide (CO_2) into solid carbonate, representing a promising approach for long-term carbon sequestration.[7] Two main methodologies used to prepare calcium carbonate are precipitation from supersaturated solutions[8] and growth by the ammonium carbonate diffusion method.[9] For both cases, the particles can grow homogeneously in the solutions or heterogeneously on seeding materials or solid substrates.

The crystal growth of calcium carbonate is known to be very complex, due to both the multiple phases and polymorphs that can act as intermediate phases and the presence of nonclassical crystal growth mechanisms (i.e., other than monomer-by-monomer addition of chemical species[10]). For example, three different pre-nuclei, ACC, vaterite, and calcite, are most commonly identified during calcite synthesis.[11] Consequently, the types of calcium carbonate polymorphs vary strongly with the synthesis conditions. A relevant nonclassical mechanism of crystallization is oriented particle attachment that proceeds by

A. F. Suzana, S. S. Lee, P. Fenter
Chemical Sciences and Engineering Division
Argonne National Laboratory
Lemont IL 60439, USA
E-mail: asuzana@anl.gov
I. Calvo-Almazán
Instituto de Nanociencia y Materiales de Aragón (INMA), CSIC - Universidad de Zaragoza
Calle de Pedro Cerbuna 9, Zaragoza 50009, Spain
W. Cha, R. Harder
Advanced Photon Source
Argonne National Laboratory
Lemont IL 60439, USA

The ORCID identification number(s) for the author(s) of this article can be found under https://doi.org/10.1002/adma.202310672

DOI: 10.1002/adma.202310672

repeated events of particle attachment along specific crystallographic directions, either through perfect crystallographic alignment or against structural discontinuities such as twin boundaries and stacking faults.[12] These different mechanisms can be distinguished by the degree of supersaturation during growth.[4] While the specific crystal growth mechanism might be expected to significantly influence the morphology, crystallinity (i.e., internal crystallographic domains), and internal atomic distortions (i.e., strain) of synthesized calcite, the possible influence of the synthesis methodology (which is intrinsically related to the growth mechanism) on the internal structure of crystals has received little attention.

Insights into the mechanisms for calcite growth can be obtained by imaging the crystallographic domains using Bragg coherent diffraction imaging (BCDI), a lensless technique for 2D or 3D reconstruction of individual nanoparticles and directly sensitive to deviatoric strain. BCDI works by illuminating a crystal with a coherent plane-wave X-ray probe and recording its diffraction pattern around a specific Bragg reflection.[13] As a diffraction experiment, only the squared amplitude of the complex Fourier signal is measured, not the phase, which gives rise to the well-known "phase problem" of crystallography.[14] In BCDI, the missing phase of the diffraction pattern is recovered mathematically, usually using iterative phase retrieval algorithms[15] that are guided by both real and reciprocal space constraints on the measurement and recovered densities.[16] The real space constraint consists of a finite support region in which the electron density of the object is allowed to exist, while the reciprocal space constraint requires that the amplitude of the diffracted wave corresponds to the square of the experimental intensity which should be oversampled.[16] The recovered object is a 3D complex-number map whose amplitude is proportional to the electron density, providing a direct image of the crystalline regions, and whose phase probes the displacement fields of the atoms in the crystalline structure with sub-Ångström sensitivity projected along the Bragg vector (G) measured during the experiment. The application of this methodology requires full illumination of the entire crystal by the coherent X-ray beam, which is typically <2 μm in size at current synchrotron beamlines.

In this paper, we use the novel imaging capabilities of BCDI to compare the external morphology and internal crystallinity of calcite particles prepared using two synthesis approaches: precipitation from highly supersaturated solutions (referred to as the precipitation from solution approach) and the ammonium carbonate diffusion approach at near-equilibrium conditions. The precipitation from the solution approach initially yielded nucleation of metastable vaterite, which transformed into euhedral calcite crystals after equilibration in a calcite saturated solution (CSS). The apparent crystallite size of calcite calculated from the X-ray diffraction (XRD) data was significantly smaller than the size of the crystals seen in the scanning electron microscopy (SEM) images, suggesting the presence of smaller domains within each particle. BCDI images directly show that the calcite precipitated from solution had a complex internal structure that contained multiple nanosized domains with effectively null electron density. The phase images also showed very pronounced displacement fields in individual domains. This inherent nanocomplexity is interpreted to be due to a nonclassical crystallization mechanism in which vaterite forms as microsized particles with nanocrystalline domains, followed by a vaterite-to-calcite transformation that preserves the original vaterite nanocrystallinity but with the expected rhombohedral shape of calcite. In contrast, calcite samples grown by the ammonium carbonate diffusion method showed an almost perfect euhedral reconstruction with less lattice strain, consistent with the expected behavior for ideal crystals synthesized under near-equilibrium conditions. These results demonstrate how imaging techniques such as BCDI can be used to make the connection between the synthesis route and the crystalline structure of individual particles.

2. Results and Discussion

2.1. Calcium Carbonate Synthesized Using the Precipitation from Solution Approach

Solutions of calcium chloride monohydrate and sodium carbonate were mixed under constant magnetic stirring in a beaker containing several pieces of Kapton films (each stripe of ≈5 × 30 mm^2 in area and ≈0.1 mm in thickness) suspended in the solution. Here, Kapton is used as a growth substrate, on which well-attached $CaCO_3$ particles grow, enabling the BCDI experiment by avoiding particle motion during the experiment. Each of these films was removed after a specific reaction time (i.e., 1–5 min), but the 5 min sample was left in contact with a CSS overnight. Additional details on the synthesis procedures are described in the "Experimental Section." Here, we compare crystallization of calcite from supersaturated solutions by homogeneous growth (i.e., crystallization in the bulk solution) and heterogeneous growth (i.e., crystallization on Kapton surfaces). After a few seconds of reaction, the solution became whitish indicating homogeneous precipitation.

Figure 1a–e shows SEM images of crystals grown by heterogeneous nucleation on Kapton films after 1, 2, 3, 4, and 5 min of reaction, respectively. For these reaction times, there is predominance of spherical/oval particles, presumably the vaterite phase. Isolated rhombohedral calcite crystals are also observed as a minor phase. The preferred formation of vaterite at the earlier stage of reaction reflects its faster formation kinetics than calcite, consistent with previous observations.[17,18] Figure S1 (Supporting Information) shows the histograms of the size distribution for the vaterite crystals shown in Figure 1a–e. The mean particle sizes for reaction times 1–5 min are 537 ± 89, 636 ± 194, 699 ± 177, 1041 ± 136, and 519 ± 139 nm, respectively. Samples reacted for 5 min (referred to as $CaCO_3$-5; Figure 1e) were kept overnight in a CSS. The SEM image of the sample after the overnight treatment (Figure 1f) shows that all particles in the $CaCO_3$-5 sample transformed into euhedral calcite crystals (referred to as the "calcite–CSS sample"). The transformation of vaterite into calcite likely occurs as the thermodynamically metastable vaterite transforms into the stable calcite particles[18] (i.e., a dissolution–reprecipitation process).

Knowledge of the solution pH during the reaction is critical to understanding changes in the concentration of various aqueous species during the reaction progress. Figure S2 (Supporting Information) shows the plot of pH measured as a function of reaction time from 1 min to 24 h (after 5 min, the stirring was stopped). The pH changes abruptly for approximately 1 min (from 9.7 to 8.3), presumably due to the formation of

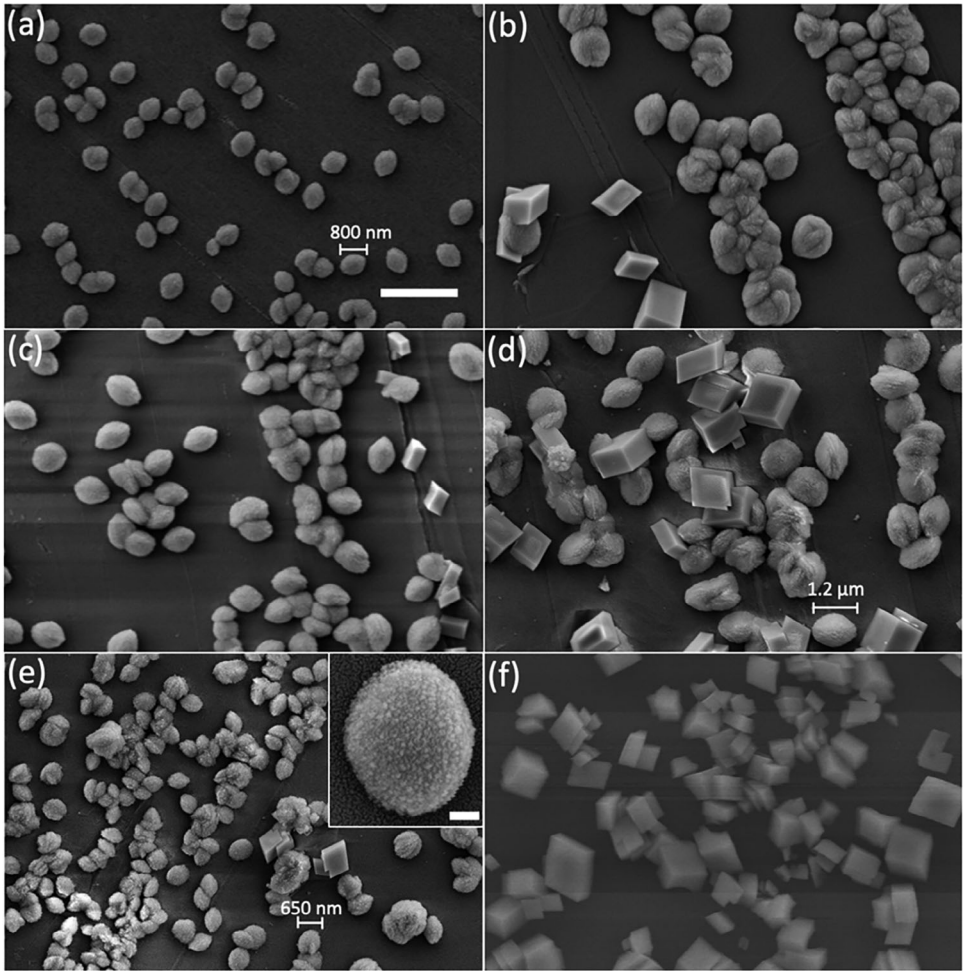

Figure 1. a–e) Representative SEM images of the calcium carbonate samples grown from supersaturated solutions on Kapton films after 1, 2, 3, 4, and 5 min of reaction, respectively, and f) after 24 h in contact with CSS. The scale bar in panel (a) represents 2 µm. The same magnification is used for panels (a)–(f). The scale bar in the inset of panel (e) is 200 nm.

metastable vaterite as an initial product. After 40 min of reaction, the pH changes very gently, indicating that near-equilibrium conditions (i.e., similar growth and dissolution rates for $CaCO_3$) were reached. This point is marked as a gray dashed line in the plot. It is important to emphasize that these changes in solution composition are controlled by the homogeneous precipitation of calcite. In contrast, the results in Figure 1 show the particles that are grown heterogeneously on Kapton. Note, however, that structural analysis based on the XRD and BCDI results discussed later in this manuscript shows that the structure and morphology of the final calcite product coming from heterogeneous as well as homogeneous growth from supersaturated solutions are similar.

Figure 2 shows the XRD of the a) $CaCO_3$-5 and b) calcite–CSS samples obtained as powder that is homogeneously precipitated in the reaction solution (see the "Experimental Section"). For the $CaCO_3$-5 sample, both vaterite and calcite phases (labeled as V and C, respectively) can be identified. For the sample further reacted in CSS, only calcite peaks are seen. These results show good agreement with the SEM images of heterogeneously grown $CaCO_3$, demonstrating that both homogeneously and heterogeneously grown crystals are formed by the same phases. XRD was performed for the homogeneously precipitated sample because it required a significant amount of powder, which was not possible to obtain with heterogeneous growth. The data analysis (described in the "Experimental Section") reveals that the Bragg peaks of the calcite–CSS sample (Figure S3b, Supporting Information) are broader than the instrumental resolution. Using the diffractometer parameters obtained from the Al_2O_3 standard (most notably an intrinsic angular resolution of $\Delta 2\theta = 0.050 \pm 0.001°$), we obtain a good fit to the calcite–CSS sample (see detail of peak fit to the calcite (104) Bragg peak in Figure S3e of the Supporting Information), which reveals an average peak width of $\Delta 2\theta = 0.177 \pm 0.008°$. This peak is 3.6-fold wider than that observed for the Al_2O_3 powder. There is no significant increase in peak width with increasing momentum transfer, Q (Figure S4a, Supporting Information), indicating that the contribution of strain in the observed width is negligible. Consequently, the finite peak width can be interpreted as, due primarily to, a finite average crystal size of 50 ± 2 nm (obtained by linear extrapolation of the width to $Q = 0$). The same analysis applied to the $CaCO_3$-5 sample shows that the calcite portion of this sample is very similar from that of the calcite–CSS sample with an average

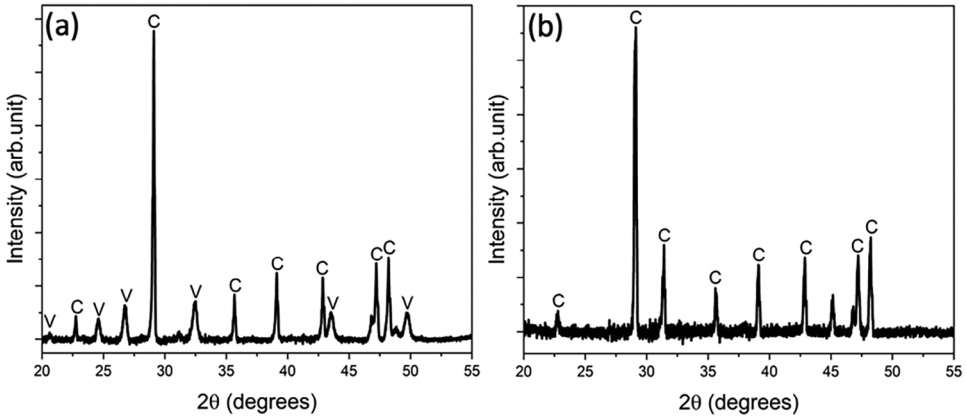

Figure 2. XRD of a) the $CaCO_3$-5 sample grown homogeneously from supersaturated solutions and b) after 24 h reaction in CSS. C and V stand for calcite and vaterite, respectively.

crystal size of 64 ± 3 nm, indicating that the 24 h annealing in CSS did not significantly alter the calcite crystallinity. In comparison, the vaterite portion of that sample has significantly broader Bragg peaks especially at higher Q (Figure S3c, Supporting Information). The peak widths show a significant increase with increasing Q (Figure S4b, Supporting Information), suggesting the presence of lattice strain. The derived vaterite particle size is 56 ± 34 nm, consistent with that for calcite.

We compare the crystal domain sizes obtained by XRD with the particle sizes observed by SEM (Figure 1). The vaterite crystalline domain size is significantly smaller than the individual spherical vaterite particles (≈1 μm in size) observed by SEM, but comparable with the size of the individual grains as seen in the inset in Figure 1e (also by ex situ atomic force microscopy, AFM; Figure S5, Supporting Information). This behavior is a common observation for nonequilibrium solid synthesis that is characterized by "primary" and "secondary" particles, corresponding to the individual crystals and their aggregates, respectively (e.g., lithium-ion battery cathode synthesis).[19] As discussed above, a similar observation is made with calcite, e.g., the crystal domain size is much smaller than the size of the crystals seen in Figure 1f. This is surprising since the observation of rhombohedral crystal shapes by SEM immediately suggests a single crystal. This observation implies that these rhombs are composed of smaller crystallite domains that are separated by grain boundaries but are grown with similar crystallographic orientations. The BCDI results discussed later in this manuscript are in accordance with this indication.

We tested the reproducibility of the calcite synthesis and stability of the particles precipitated from solution. Synthesis of calcium carbonate particles in a reproducible manner and phase/shape control is challenging, and production protocols often lead to sample variability. Figure S6 (Supporting Information) shows a SEM image of the $CaCO_3$-5 particles prepared from a separate batch under the same conditions as that shown in Figure 1e. The characteristic rhombohedral and spherical shapes of calcite and vaterite crystals, respectively, demonstrate that our approach is reproducible in terms of phase whereas the average size of the crystals varies by a factor of about 2. Another important criterion is the preservation of the well-defined particle size after extended times (e.g., for studies of reactions using these synthesized calcite rhombs). Importantly, the particles were found to be stable over time, suggesting that it reached equilibrium conditions after a few days. This was verified by leaving the beaker containing the sample $CaCO_3$-5 untouched for several days. After a few days, the calcite particle size is preserved in the solution, as seen by SEM images of these particles after 3 and 6 days (Figure S7a,b, Supporting Information), respectively. The particle size is in the range of 1–4 μm.

2.2. Calcium Carbonate Synthesized Using the Ammonium Carbonate Diffusion Approach

In order to understand how the growth conditions influence internal crystallinity of calcite, we also synthesized calcite crystals following the well-known ammonium carbonate diffusion approach. **Figure 3a** shows a schematic describing the experimental setup; a drop of calcium chloride solution is placed upside down in a gold thin film substrate covered with self-assembled monolayers (SAMs), which is exposed to the vapor released by the decomposition of ammonium carbonate in a sealed vessel (see the "Experimental Section" for details). In our case, the reaction took place in a plastic Petri dish placed inside the sealed container. Figure 3b shows a SEM image of this sample. We can clearly identify the characteristic rhombohedral crystals for calcite, and a minor fraction of spherical particles, characteristic of vaterite (indicated by black arrows). Most of the calcite crystals are in the 2–15 μm size range and well dispersed on the gold substrate. A significant portion of the crystals expose their (104) planes aligned parallel to the substrate surface. These images and the BCDI experiment (refer to the following sections) revealed that the synthesis protocol using the SAMs' approach is appropriate to produce good quality calcite crystals on the gold SAM substrate (called "calcite–SAM" hereafter).

2.3. BCDI Characterization of the Internal Structure of the Calcite Particles

BCDI results for calcite–CSS and calcite–SAM samples, respectively, are shown in **Figure** 4a,b in comparison with

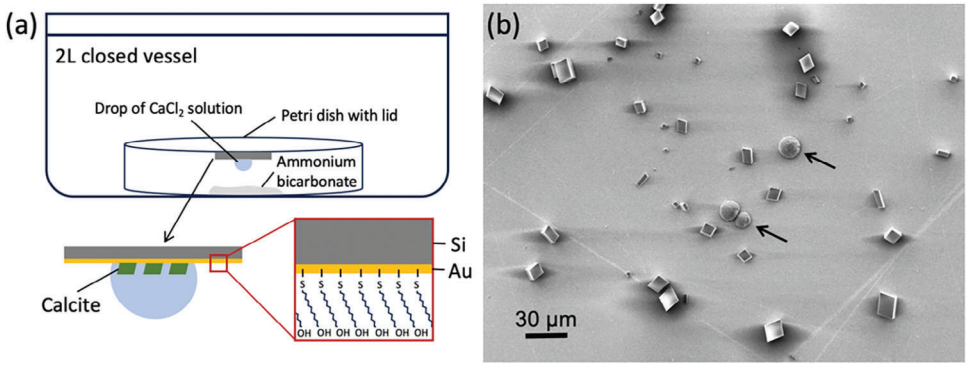

Figure 3. a) Schematic diagram of the experimental setup used to synthesize calcite particles using the ammonium carbonate diffusion approach. The synthesis was adapted from previous works.[20–22] b) SEM image of the calcite crystals synthesized on the gold thin film covered with SAMs (shown schematically in panel (a)). The black arrows point to vaterite particles.

high-magnification SEM images of the euhedral calcite crystals that were synthesized by the same approaches. Unlike the visual similarity shown in their SEM images, their 3D (104) Bragg peak patterns are dramatically different. The calcite–SAM sample shows a strong and well-defined diffraction peak center and clearly defined streaks of intensity corresponding to the surface facets whereas the calcite–CSS sample shows a much more complex diffraction pattern, the latter result being unexpected. In the beginning of our experiment, we tested the sample stability by measuring multiple rocking curve scans for the same particle. Figure S10 (Supporting Information) shows four repeated scans of one particle (not the same presented in Figure 4), in a total exposure time of 27 min. The intensity was stable over time, indicating that there were no changes in the crystalline structure of the particle during the measurements.

Before the BCDI experiment, we characterized the Kapton films containing the calcite–CSS with SEM in order to map the 2D concentration of particles on the membranes. Figure S8 (Supporting Information) displays a typical SEM image with a large field of view of the calcite–CSS sample, showing spatial variations in the concentration on the Kapton membrane (note that the crystals shown in the SEM images in this paper are not the same as those measured in the BCDI experiment). During the BCDI experiment we focused on regions with a relatively high particle concentrations using an integrated confocal microscope at the beamline. It was time consuming to find oriented crystals and when found, for many cases, the diffraction had weak intensity with no apparent fringes that would be characteristic of single-crystalline euhedral particles (Figure 4a). When well-defined fringes were present in the diffraction pattern, more than one set of fringes was seen, slightly misaligned with each other. For a few particles, we could see more than one center for the diffraction peak. This is an indication of the presence of domains in these particles, for example, separated by twin boundaries. This can be due to the possibility that crystals grew on top of each other with some degree of misorientation. Indeed, we can see in

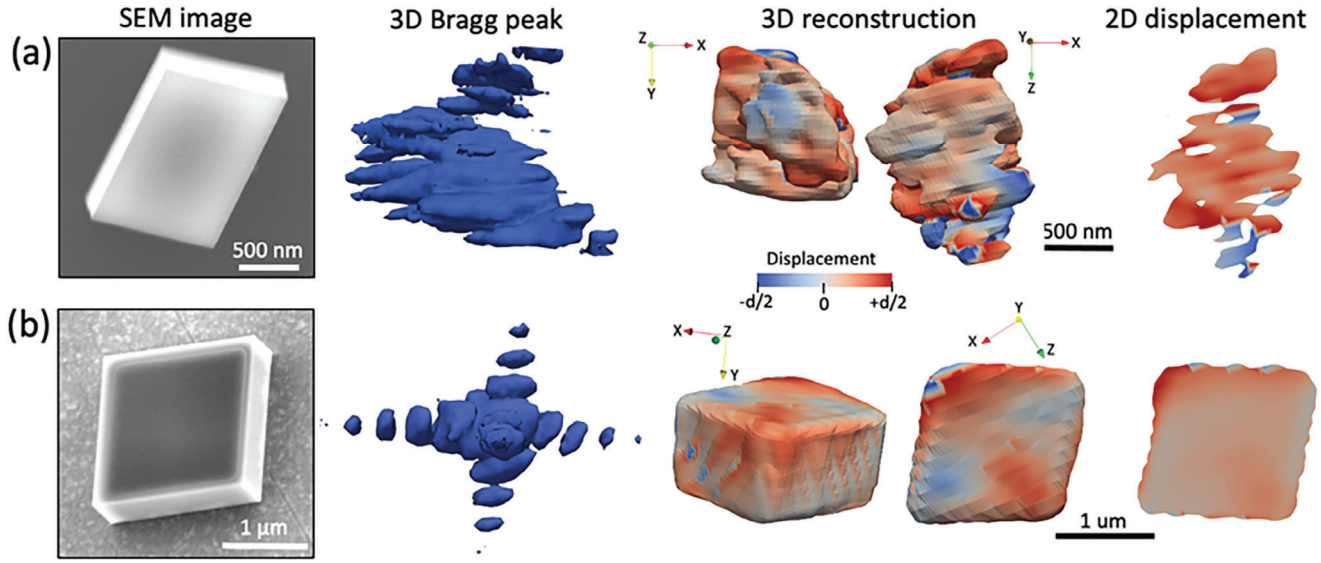

Figure 4. From left to right: SEM images of individual calcite crystals, 3D representation of the (104) Bragg peaks, two different views of the BCDI reconstruction, and cross-sectional views of the second 3D image for calcite that were a) precipitated from supersaturated solution, and b) synthesized using the ammonium carbonate approach. The plot is colored according to the displacement field along the [104] direction.

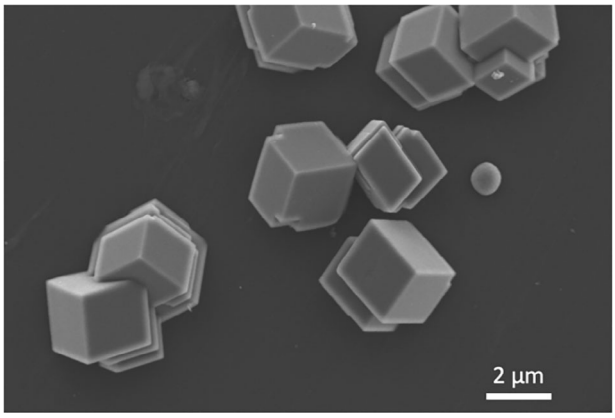

Figure 5. SEM image of the sample $CaCO_3$-5, showing calcite crystals that are twinned and/or overgrown.

SEM images taken before the experiment (grown using the same synthesis route but in a different batch) that there was a high concentration of particles that appeared to consist of one rhomb growing on top of another, or possibly as intergrown rhombs (**Figure 5**, also seen in a subset of particles in Figure 1f). The presence of multiple crystallites within a given rhomb (separated by small-angle grain boundaries) would explain the complex speckly diffraction pattern seen for several particles.

The presence of sharp grain boundaries within a given crystal is known to be challenging to image using the phasing algorithms that are used to invert these data.[23,24] Here we show the reconstructions that were reproducible regarding successive reconstructions using the same parameters. In comparison, the analyses of other particles were not reproducible, a common problem in the inversion when the reciprocal space data are too speckly, or it does not satisfy the oversampling constraint for robust data inversion. The reproducibility of the reconstructions of the calcite–CSS sample was tested by performing multiple reconstructions of another particle measured in the BCDI experiment, using the same initial parameters. Figure S9 (Supporting Information) shows the resulting 3D particle of two of these reconstructions, and 2D slices taken close to the center of the particle. Although the morphology of the particle is not exactly the same, both reconstructions show a pronounced displacement field and null electron density domains. For both reconstructions, we can see that the strong positive displacement field occurs in the same region within the image of the reconstructed particle (red-colored region in Figure S9 in the Supporting Information, pointed by black arrows). In comparison, BCDI measurements of the calcite–SAM samples were relatively straightforward, except for the challenge that a significant portion of the particles were larger than the limit for the oversampling criteria to be met, and it was time consuming to find smaller (≈2 μm) crystals that were fully illuminated.

Two different external views and a cross section of the 3D reconstruction (taken for the second view) are displayed in Figure 4 for the calcite–CSS and calcite–SAM samples, where the color represents the recovered displacement field (see the Supporting Information for details). The phase represents the projection of atomic displacements onto the *G* vector measured with respect to an unstrained reference structure, ⟨104⟩ in the case of our experiment, where red-colored regions represent positive values of the atomic displacements along the **G** vector direction, and blue-colored regions are negative values, i.e., along the opposite direction. For the calcite–CSS sample, the reconstructed particles present regions with null electron density, implying that any material present in these regions does not satisfy the (104) Bragg condition measured during the experiment. This may be due to angular misalignment that was greater than the rocking scan range (± 0.3°), or this region may have an inclusion with a different crystalline structure (e.g., vaterite), or assembly of smaller nanocrystallites. In principle, this region may also correspond to a vacancy in the crystal. Since the SEM images show that the calcite crystals have continuous rhombic facets with no noticeable nanoscale defects, we think that it is most likely that these apparent vacancies reflect the nanocrystalline texture of these individual calcite rhombs.

It is also notable that the recovered phase is "wrapped" in a few regions of the particles (where there is a direct change from blue to red) especially for the calcite–CSS sample. This occurs when the local phase changes from $+\pi$ to $-\pi$ (or vice versa) because the phase is only defined modulo $\pm\pi$, and implies that the net displacement in the calcite crystalline structure exceeds one *d*-spacing (3.0357 Å, a nominal value for the (104) reflection) within the range. Therefore, we can conclude that the crystalline structure of these synthesized rhombs is very defective. This can be due to numerous defects in the crystalline structure such as strain and crystalline rotation. For example, the present measurements cannot uniquely discern rotation from shear strain having measured just one Bragg peak in the BCDI experiment. A minimum of three Braggs peaks is required to be able to construct the nine components of the full strain tensor and the rigid-body rotation, as described before.[25]

Identification of such deformations in the crystalline structure is crucial for minerals. For instance, San et al.[26] identified the presence of twins, partial dislocations, and stacking faults in aragonite crystals, using mainly transmission electron microscopy. It was concluded that the twin density depends on the mineral-formation environment, e.g., temperature and pressure. Similar studies[27–29] of biogenic calcite identified the presence of domains and lattice distortions, which were attributed mainly to the incorporation of organic molecules in the crystalline structure. These findings may help in designing materials with optimized strength and toughness. BCDI technique can also be used to identify defects in the internal structure, with the main advantages of 3D defects mapping, and in situ/operando characterization, as shown previously for a wide range of materials such as minerals,[20] batteries,[30] and catalysts.[31]

Unlike the 3D Bragg peaks measured for the calcite–CSS particles precipitated from solution, the particle synthesized by the ammonium carbonate diffusion approach (calcite–SAM) presents sharp fringes in three different directions representing the diffraction interference pattern of the three sets of parallel facets composing the euhedral calcite crystal (Figure 4b). The reconstructed particle shape clearly recovers the expected rhombohedral shape along with phase gradients indicating the presence of defects without any null electron density regions, consistent with the results reported in previous works.[20–22] These observations are in stark contrast to the calcite–CSS crystals that were grown in highly supersaturated conditions, which have a

highly defective internal structure despite the fact that the external shapes determined by SEM match the expected crystal morphology. Figure S11 (Supporting Information) shows a phase line plot over the dashed lines shown in the 2D slices for calcite–CSS and calcite–SAM particles (left and right, respectively). While the phase variation is more pronounced for the calcite–CSS particle, it is clearly smoother for the calcite–SAM particle. The irregular pattern with peaks and valleys seen for the calcite–CSS sample is a clear indication of the presence of these domains. The size of them (one example is shown in the figure, ≈60 nm) is in good agreement with the domain size obtained from the XRD peak shape analysis (≈50 nm). A similar phase plot of a slice taken for the calcite–CSS sample is shown in Figure S12 (Supporting Information) for a line that is drawn across four null electron density regions (1–4 in the figure). The phases before and after regions 1 and 2 have roughly the same slope, indicating that the calcite grains are separated by an insertion of a twisted inclusion domain (null electron density regions) between domains of same orientation.

2.4. Reaction Pathway Proposed for the Calcite Precipitated from Solution

The significant distinctions in the internal structures between calcite–CSS and calcite–SAM reflect differences in the crystallization pathway controlled by the synthesis approaches used for the calcite production, ammonium carbonate diffusion[30,31] versus precipitation from solution. Based on the SEM/XRD results and on the BCDI reconstructions, we conclude that complex nanocrystallinity of the calcite–CSS sample is a fingerprint of nonclassical crystal growth.[10] At low supersaturation, nucleation events are rare, and a monomer-by-monomer pathway is predicted by classical theories. In contrast, the rate of particle nucleation is substantially increased at higher supersaturation, and the subsequent crystal growth tends to be particle based, e.g., through the Ostwald ripening or a coalescence process.[10] The initial saturation indices for vaterite and calcite were 2.3 and 2.8 (calculated using Minteq; see the "Experimental Section" for details), respectively, leading to the formation of these phases, with predominance of the metastable vaterite because of its faster formation kinetics than calcite.[32] The growth of larger crystals through the coalescence of smaller nanoparticles has been reported for biominerals.[33] For vaterite, the micrometer-sized particles that initially formed in the supersaturated solution (Figure 1e) appeared as aggregates of smaller primary vaterite crystals with no apparent crystallographic arrangements. From the electron microscopy images of calcite, shown here, the particles after equilibration in CSS occurred as euhedral crystals, indicating that the coalesced particles either were crystallographically aligned with each other or underwent a secondary ripening process. However, our BCDI work shows the complex diffraction pattern and the presence of domains for all the crystals, which is strong evidence of structural misalignment and/or defects within the particles. In addition, we found that there were no vaterite crystals after the equilibration in CSS, indicating the transformation of metastable vaterite into stable calcite. Here, we would like to highlight that these conclusions rely on the use of multiple techniques (i.e., SEM, XRD, and BCDI) that have complementary sensitivities to crystalline structure, morphology, and atomic displacements.

The similarity of the initial vaterite and final calcite particle sizes (observed by SEM), along with their similar (but smaller) intrinsic crystal sizes (observed by XRD), suggests that the observed nanocrystallinity of calcite was inherited from the nanocrystalline vaterite. As an initial step, individual nanoscale vaterite crystals can transform into calcite, maintaining both the nanocrystallinity and the overall particle size (**Figure 6**, top row). We also observe that the vaterite particle size depends upon reaction time (Figure S1, Supporting Information), suggesting that interparticle exchange may also contribute to the particle evolution. This suggests a dissolution–reprecipitation mechanism (Figure 6, bottom row).

One of the plausible mechanisms for maintaining the structural resemblance is an interface-coupled dissolution–precipitation reaction, similar to a mineral replacement.[34] In this process, the dissolving parent phase can act as the substrate for the nucleation and growth of the secondary phase, i.e., vaterite and calcite, respectively, in this case. A main structural constraint that controls the spatial extension of this transformation is the volumetric change between the initial and final phases. The molar volume of vaterite is only slightly larger than that of calcite (i.e., ≈2% between 37.7 and 36.9 cm^3 mol^{-1}, which corresponds to ≈0.7% compressive strain). If the composition of the materials is preserved in the reaction, the transformation yields slight volume contraction, which can be readily accommodated within the nanometer-sized primary particles. These replacing calcite nanoparticles can grow into larger crystals through the rearrangement of the particle orientation within the aggregates followed by a crystallographically controlled nearly oriented attachment process. Alternatively, the expected volume changes in the individual calcite nanoparticles may alter the integrity of the micrometer-sized aggregates, which in turn leads to the dissociation of the aggregates followed by re-assemblage of nanocrystalline calcite into larger crystals (Figure 6, bottom row).

Another important consideration regards the comparison between the samples synthesized heterogeneously on Kapton films and homogeneously in the solution. Figure S13 (Supporting Information) shows a SEM image taken for the $CaCO_3$-5 homogeneously grown sample. Both vaterite and calcite phases can be identified. The primary difference between this and the heterogeneously grown sample (Figure 1e) is the particle size; the $CaCO_3$-5 homogeneously grown particles are bigger (around ≈2 µm), although this is consistent with the batch-to-batch variation of crystal size, as pointed out above. Both XRD (collected for the homogeneously grown sample) and BCDI results (collected for the heterogeneously grown sample) show the presence of domains in the sample, indicating that these samples are generally similar from a structural point of view.

3. Conclusions

In this work, we showed how the nanocrystallinity of calcite is sensitive to the specific synthesis methodology. Calcium carbonate particles were synthesized using two approaches: direct precipitation from solution and the ammonium carbonate diffusion methodology. For the crystals precipitated from solution, after 5 min of reaction, there is a mixture of both vaterite and calcite, and

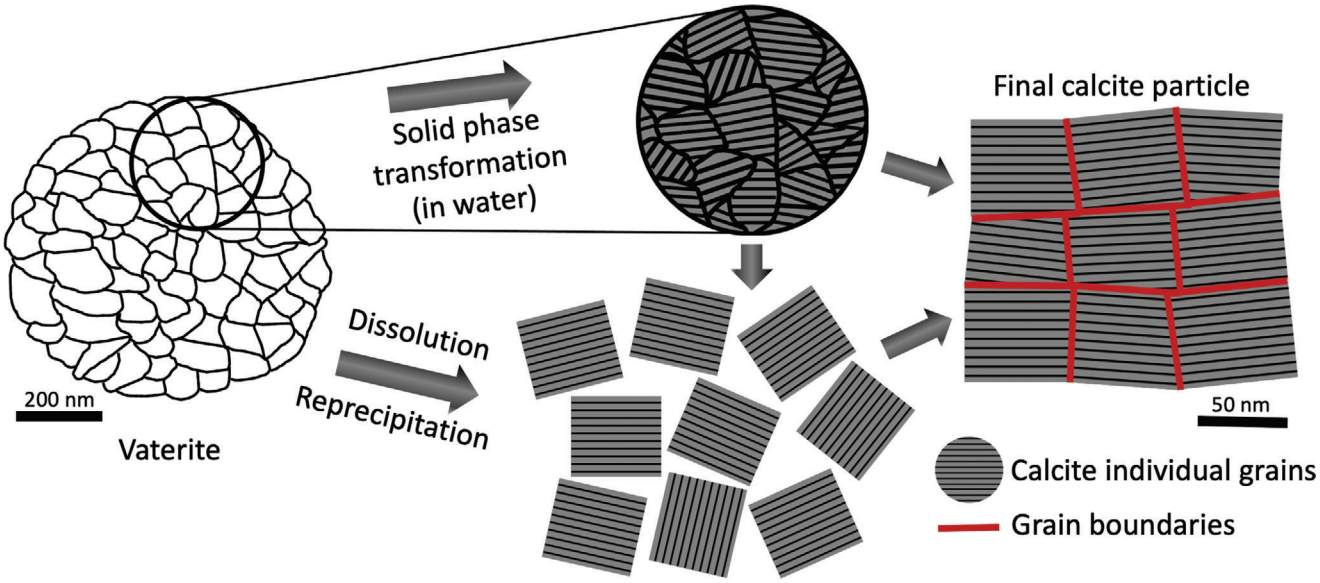

Figure 6. Schematic of the proposed reaction pathways inferred for calcite crystals synthesized by the precipitation from solution approach based on the SEM, XRD, and BCDI results. Calcite and vaterite are indicated in gray and white, respectively. Two pathways are proposed: a solid phase transformation (top) where the primary vaterite particles transform into calcite and then subsequently evolve morphologically into a rhomb shape, and a dissolution/reprecipitation transformation (bottom) where vaterite particles dissolve and reprecipitate as small calcite crystallites that then merge through nearly oriented particle attachment, as described earlier.[10] For either mechanism, the final calcite particle with domains is represented on the right.

after exposure to CSS overnight, only the calcite phase is present, as confirmed by SEM imaging and powder XRD. This shows that the phase transformation is highly dependent on the particles' exposure time to saturation conditions, where metastable vaterite transformed into stable calcite. For the particles obtained by ammonium carbonate diffusion, there is a predominance of the calcite phase. BCDI measurements show that the calcite particles in the calcite–CSS sample have crystalline domains with a very pronounced atomic displacement field distribution, while those in the calcite–SAM sample are uniformly crystalline. We interpret the appearance of the nanocrystalline domains as a fingerprint inherited from original vaterite nanocrystals, which transformed to calcite via a nonclassical crystallization mechanism, i.e., oriented particle attachment. In contrast, the calcite images and associated displacement field map of the calcite–SAM sample were smoother, and the recovered shape was very similar to the rhombohedral particles seen by SEM, indicating that these were true single crystal grains.

The BCDI results provide new information on the internal structure of the synthetic calcite crystals, showing that crystals precipitated from solution can be highly defective, even though the SEM images showed euhedral rhombohedral crystals. Therefore, the combination of these imaging techniques was essential for unveiling the morphology evolution, and the defects distribution, and linking these with calcite crystallization mechanisms based on oriented particle attachment for the calcite–CSS sample. The final structure and morphology have direct implications in the properties of minerals. Although the relationship between domains and reaction pathways has received little attention for calcite, the presence of these domain boundaries certainly may play an important role in chemical reaction pathways as they can be channels for increased reactivity. This increased reactivity can influence reactant transport of heavy metal ions in natural systems, for example, as that is controlled by the buffering of calcium carbonate. We expect two areas where the present results may be useful in understanding mineral reactivity. First, grain boundaries of calcium carbonate have been shown to be an effective fluid pathway for the progression of the reaction front in the replacement reaction of calcium carbonate by calcium phosphate.[35] Second, the presence of lattice distortion in the crystalline structure will likely change the surface energies, and this can potentially facilitate processes such as the incorporation of ions/molecules, adsorption, and dissolution. Our study demonstrates that the internal grain boundary structure of visibly rhombohedral calcite particles may differ dramatically depending on the synthesis approach, and we also demonstrate that the BCDI approach provides a direct way to probe these features so that structure–property relationships can be determined. We are currently studying the relationship between the domain boundaries and reactivity of calcite crystals, and preliminary results show that the dissolution reaction on calcite starts preferably on grain boundaries. Our results may also be relevant to other fields such as catalysis. The presence of grain boundaries inside particles might also enhance the catalytic activities of the materials by increasing the reactive surface areas. In detail, these activities will be further influenced by the connectivity of the internal interfaces to the external surfaces, controlling the transport of the reactants into the channels.

4. Experimental Section

Synthesis of Calcium Carbonate Using the Precipitation from Solution Methodology: Calcium carbonate synthesis methodology was adapted from an approach reported before.[3] In a typical synthesis, 20 mL of

20 mM $CaCl_2{\cdot}H_2O$ (calcium chloride monohydrate) solution was mixed with 4 mL of a 20 mM Na_2CO_3 (sodium carbonate) solution in a beaker under magnetic stirring. The Ca:CO_3 molar ratio was 5:1. For the BCDI experiment and the SEM imaging shown in the main manuscript (except the ones shown in Figure 3), $CaCO_3$ particles were grown on Kapton films that were glued on the internal walls of the beaker. After 5 min of magnetic stirring, the reaction was stopped, and the Kapton films were removed from the beaker; this sample is referred to as $CaCO_3$-5 in this manuscript. For another set of samples, the Kapton films (containing $CaCO_3$-5) were placed in another beaker containing CSS and left overnight. This sample was called "calcite–CSS". CSS was prepared by reacting calcite powder (from Chihuahua, Mexico) in deionized water. The bottle containing this solution was kept on a shaker table for 1–2 months. During the reaction, the sample was maintained in contact with air (through a paper membrane). After the reaction, the aqueous solution was obtained by filtration through 0.45 µm membrane.

Synthesis of Calcite Using the Ammonium Carbonate Diffusion Approach: The synthesis procedure was adapted from previous works.[20–22] Hydroxyl-terminated SAMs on gold thin film were used as substrate to synthesize calcite mostly {104} oriented. SAMs were prepared on a commercial silicon wafer coated with a 50 nm gold film. A thin chromium adhesion layer (2–7 nm) was present between the silicon and gold. This substrate was then immersed in a 1 mM 11-mercapto-1-undecanol solution in ethanol at room temperature overnight in the dark. The membrane was then carefully rinsed with ethanol and dried with ambient air. The calcite synthesis protocol used was the ammonium carbonate diffusion methodology: ≈1 g of ammonium bicarbonate was placed in a Petri dish inside an ≈2 L vessel. Then a drop of 15 mM calcium chloride solution was placed on the gold SAM substrate and left upside down right above the ammonium carbonate powder (Figure 3a). In preliminary tests, it was found that the volume of the drop did not influence the composition, concentration, and size of the final particles, therefore the volume of the calcium chloride drop was not controlled. The vessel was closed for the reaction occurrence, and after 20 min of reaction, the vessel was open, and the gold substrate was carefully rinsed with ethanol and dried with ambient air. The dried sample, named calcite–SAM in this manuscript, was used for the BCDI experiment. The CSS overnight treatment was not done for this sample because the final phase is mostly calcite.

Scanning Electron Microscopy: SEM imaging was done using a Zeiss Gemini SEM model operating at either 5 or 10 kV in the secondary electrons' detection mode. $CaCO_3$-5 and calcite–CSS samples were prepared by either grown directly on Kapton membranes (as described above), or by dispersing a solution containing $CaCO_3$ powders on silicon wafer membranes, extracted directly from the reaction beaker. The calcite–SAM sample was measured after it was dried from the ethanol rinsing procedure. All samples were carbon- or Au-coated before SEM imaging.

Powder X-Ray Diffraction: XRD measurements were carried out using a Bruker D8 Advance equipment, Cu as the radiation source operating at voltage and current of 40 kV and 40 mA, respectively. The diffraction scan parameters were 2θ in the range of 10°–80°, scan steps of 0.01°, and an exposure time of 1 s for each point. A diffuse background was subtracted using a spline function. For the $CaCO_3$-5, the sample preparation consisted of centrifuging the final dispersion for 20 min at 15 000 rpm. The wet powder deposited on the bottom of the centrifugation tube was placed in the XRD sample holder and left to dry for a few hours under ambient conditions. For the calcite–CSS, the sample preparation consisted of drying the sample overnight under vacuum at 40 °C.

Peak Shape Analysis: Powder diffraction data from three samples were analyzed to understand the source of broadening observed in the XRD data of the calcite samples. Characterization of the diffractometer system was performed with an Al_2O_3 powder standard having an average crystal size of 5–10 µm in diameter by 2–3 µm in thickness. Multiple Bragg peaks were observed within the angular range of $20° < 2\theta < 55°$, each showing a characteristic splitting due to the $k\alpha_1$ and $k\alpha_2$ lines from the Cu anode source having wavelengths of 1.5406 and 1.5444 Å (Figure S3a, Supporting Information). Initial fits to these data used a Gaussian line shape without any constraints on the relative positions, widths, and intensities of the observed Bragg peaks. These results provided a direct calibration of the relative intensity of the $k\alpha_1$ and $k\alpha_2$ lines ($I_{k\alpha 2} = I_{k\alpha 1}/1.9$) of the experimental data and the 2θ-dependent peak splitting which had a linear functional dependence, $\Delta 2\theta\ (°) = 0.037\ Q_i$, where Q_i is diffraction peak position (in units of $Å^{-1}$). With these parameters fixed (and with the double peak position, peak width, and overall intensity unconstrained), the fit of the Al_2O_3 XRD data was adequate ($\chi^2 = 37$, a highlight of the Al_2O_3 (104) Bragg peak is shown in Figure S3d in the Supporting Information), and reproduced the individual peak line shapes. The systematic variation of the peak widths with momentum transfer (Figure S4a, Supporting Information) leads to an average peak width of 0.0026 $Å^{-1}$. The Q-dependent peak width was fit using a linear function to obtain the peak width extrapolated to $Q = 0$, $\Delta Q_0 = 0.0026 \pm 1.3\text{E-}4\ Å^{-1}$, corresponding to an effective real-space resolution of $2\pi/\Delta Q_0 = 2400$ Å.

These experimental parameters were used to analyze the $CaCO_3$ powder diffraction patterns. The fit to the calcite–CSS data had a quality of fit of $\chi^2 = 1.47$. These data showed no evidence for a measurable increase in peak width with increasing momentum transfer, Q, and the peak width extrapolated to $Q = 0$ was $\Delta Q_0 = 0.0127 \pm 4.0\text{E-}4\ Å^{-1}$. Since this was larger than the experimental resolution, it was concluded that it corresponded to an average crystal size of $2\pi/\Delta Q_0 = 50$ nm. The same analysis of the $CaCO_3$-5 sample had a quality of fit ($\chi^2 = 3.1$) and had an average peak width of $\Delta 2\theta = 0.17°$. Again, there was no evidence for a measurable increase in peak width with increasing momentum transfer, Q (Figure S4b, Supporting Information), and the crystal size inferred from these data was 64 nm. The vaterite portion of the sample showed diffraction peaks that were both wider (Figure S3c, Supporting Information) and the widths increased with momentum transfer, Q (Figure S4b, Supporting Information). The average Bragg peak width was $\Delta 2\theta = 0.35°$, and the extrapolated width at $Q = 0$ was $\Delta Q_0 = 0.011 \pm 0.0014\ Å^{-1}$, similar to that observed for the calcite material. From the intercept an average vaterite domain size was obtained as $2\pi/\Delta Q_0 = 56$ nm.

Atomic Force Microscopy: The surface morphology of $CaCO_3$ polymorphs was characterized by a Cypher-ES atomic force microscope (Asylum Research, Oxford Instruments). An AC55TS (Oxford Instruments) tip with the resonant frequency of 2.15 MHz, a spring constant of 207 N m^{-1}, and a nominal tip radius of 7 nm was used in tapping mode.

BCDI Experiment: The measurement was done at 34-ID-C beamline at Advanced Photon Source (APS) in two different experiments. For both experiments, a double-crystal monochromator was used to select the energy of 10 keV, and Kirkpatrick–Baez (KB) mirrors were used to focus the beam down to sizes between 1.5 and 2.0 $µm^2$. The rocking curves (sequence of 2D diffraction patterns) for the (104) reflection of calcite were recorded using a Medipix detector, 512 × 512 pixels, 55 × 55 $µm^2$ pixel size, placed 2 m from the sample. For the calcite–CSS sample shown in this manuscript, the rocking curve was collected using a step size of 0.01 (60 points, $\Delta\theta = \pm 0.3°$), with either 2 or 10 s of exposure time, depending on the particle. For the calcite–SAM sample, the rocking curve parameters had a step size of 0.005 (40 points, $\Delta\theta = \pm 0.1°$), with 30 s of exposure time. The oversampling ratio in the case of the sample precipitated from solution was 3 (considering a 1.5 µm object), and for the sample coming from the ammonium bicarbonate approach it was 2.25 (considering a 2.0 µm object). We would like to highlight here that the oversampling ratio criteria was not met in the rocking curve direction, where this value was 1.2 for the calcite–CSS particle, and 1.7 for calcite–SAM particle. However, Figure S14 (Supporting Information) shows BCDI results of a different calcite–CSS particle measured during this experiment where the oversampling criteria in the rocking curve direction were met, and the same features were seen (null electron density regions and very pronounced atomic displacement field regions). Also, the fact that the reconstruction of calcite–SAM clearly recovers the expected rhombohedral shape demonstrates that this does not have an effect in the final answer.

BCDI Reconstruction: The phase retrieval algorithm was initiated with 20 error reduction (ER) iterations, followed by 180 hybrid–input–output (HIO) iterations,[36] alternating with each other in a total of 620 iterations, starting from random phases. A guided approach method[37] was used, with five populations and five generations. The shrink–wrap approach was used for the reconstruction process, with a threshold of 0.10

as the support constraint.[38] The trivial phase corrections were applied to these data: diffraction peak centering, the corresponding phase offset, and global phase ramp. The reconstructed images were plotted as isosurfaces in 3D using the software Paraview.[39]

Solid Saturation Index Calculation: The thermodynamic stabilities of the $CaCO_3$ polymorphs in the experimental solutions were calculated using the Geochemist's Workbench software package with the Minteq database.[40] All solutions were assumed to be in equilibrium with atmospheric CO_2 (≈420 ppm). The saturation index (SI) of a solid phase was calculated as

$$SI = \log_{10}\left(\frac{a{Ca^{2+}} \cdot a{CO_3}^{2-}}{K_{sp}}\right) \quad (1)$$

where $a{Ca^{2+}}$ and $a{CO_3}^{2-}$ are the activities of Ca^{2+} and ${CO_3}^{2-}$ ions, and K_{SP} is the equilibrium constant of a $CaCO_3$ polymorph (i.e., $10^{-8.48}$, $10^{-8.36}$, and $10^{-7.91}$ for calcite, aragonite, and vaterite, respectively).[41]

Supporting Information

Supporting Information is available from the Wiley Online Library or from the author.

Acknowledgements

This work was funded by the U.S. Department of Energy, Office of Science, Office of Basic Energy Sciences, Geosciences program (FWP 57814) under Contract DE-AC02-06CH11357 to UChicago Argonne, LLC as operator of Argonne National Laboratory. The BCDI experiment was performed at Beamline 34-ID-C at the Advanced Photon Source, Argonne National Laboratory. This research used resources of the Advanced Photon Source, a U.S. DOE Office of Science User Facility operated for the DOE Office of Science by Argonne National Laboratory under Contract No. DE-AC02-06CH11357.

Conflict of Interest

The authors declare no conflict of interest.

Data Availability Statement

The data that support the findings of this study are available from the corresponding author upon reasonable request.

Keywords

ammonium carbonate diffusion, Bragg coherent diffraction imaging, calcium carbonate, defects, precipitation from solution

Received: October 13, 2023
Revised: April 17, 2024
Published online:

[1] Y. Ding, Y. Liu, Y. Ren, H. Yan, M. Wang, D. Wang, X. Y. Lu, B. Wang, T. Fan, H. Guo, *Powder Technol.* **2018**, *333*, 410.
[2] Y. U. T. Gong, C. E. Killian, I. C. Olson, N. P. Appathurai, A. L. Amasino, M. C. Martin, L. J. Holt, F. H. Wilt, P. U. P. A. Gilbert, *Proc. Natl. Acad. Sci. USA* **2012**, *109*, 6088.
[3] Y. Wang, Y. X. Moo, C. Chen, P. Gunawan, R. Xu, *J. Colloid Interface Sci.* **2010**, *352*, 393.
[4] Y. S. Han, G. Hadiko, M. Fuji, M. Takahashi, *J. Cryst. Growth* **2005**, *276*, 541.
[5] L. Qi, J. Li, J. Ma, *Adv. Mater.* **2002**, *14*, 300.
[6] Z. Zou, I. Polishchuk, L. Bertinetti, B. Pokroy, Y. Politi, P. Fratzl, W. J. E. M. Habraken, *J. Mater. Chem. B* **2018**, *6*, 449.
[7] R. Chang, S. Kim, S. Lee, S. Choi, M. Kim, Y. Park, *Front. Energy Res.* **2017**, *5*, 1.
[8] P. G. Koutsoukos, C. G. Kontoyannis, *J. Chem. Soc., Faraday Trans. 1* **1984**, *80*, 1181.
[9] J. Ihli, P. Bots, A. Kulak, L. G. Benning, F. C. Meldrum, *Adv. Funct. Mater.* **2013**, *23*, 1965.
[10] J. J. De Yoreo, P. U. P. A. Gilbert, N. A. J. M. Sommerdijk, R. L. Penn, S. Whitelam, D. Joester, H. Zhang, J. D. Rimer, A. Navrotsky, J. F. Banfield, A. F. Wallace, F. M. Michel, F. C. Meldrum, H. Colfen, P. M. Dove, *Science* **2015**, *389*, aaa6760.
[11] L. Bergwerff, L. A. van Paassen, *Crystals* **2021**, *11*, 1318.
[12] R. L. Penn, J. F. Banfield, *Science* **1998**, *281*, 969.
[13] I. Robinson, R. Harder, *Nat. Mater.* **2009**, *8*, 291.
[14] H. Hauptman, *Proc. - Indian Acad. Sci., Chem. Sci.* **1983**, *92*, 291.
[15] M. A. Pfeifer, G. J. Williams, I. A. Vartanyants, R. Harder, I. K. Robinson, *Nature* **2006**, *442*, 63.
[16] J. Miao, D. Sayre, *Acta Crystallogr.* **2000**, *56*, 596.
[17] J. D. Rodriguez-Blanco, S. Shaw, L. G. Benning, *Nanoscale* **2011**, *3*, 265.
[18] N. Spanos, P. G. Koutsoukos, *J. Cryst. Growth* **1998**, *191*, 783.
[19] C. Deng, L. Liu, W. Zhou, K. Sun, D. Sun, *Electrochim. Acta* **2008**, *53*, 2441.
[20] J. N. Clark, J. Ihli, A. S. Schenk, Y. Y. Kim, A. N. Kulak, J. M. Campbell, G. Nisbet, F. C. Meldrum, I. K. Robinson, *Nat. Mater.* **2015**, *14*, 780.
[21] J. Ihli, J. N. Clark, A. S. Côté, Y. Kim, A. S. Schenk, A. N. Kulak, T. P. Comyn, O. Chammas, R. Harder, D. M. Duffy, I. K. Robinson, F. C. Meldrum, *Nat. Commun* **2016**, *7*, 17.
[22] J. Ihli, J. N. Clark, N. Kanwal, Y. Y. Kim, M. A. Holden, R. J. Harder, C. C. Tang, S. E. Ashbrook, I. K. Robinson, F. C. Meldrum, *Chem. Sci.* **2019**, *10*, 1176.
[23] J. R. Fienup, *J. Opt. Soc. Am. A* **1987**, *4*, 118.
[24] W. McBride, N. L. O'Leary, L. J. Allen, *Phys. Rev. Lett.* **2004**, *93*, 22.
[25] M. C. Newton, S. J. Leake, R. Harder, I. K. Robinson, *Nat. Mater.* **2010**, *9*, 120.
[26] X. San, M. Gong, J. Wang, X. Ma, R. Dos Reis, P. J. M. Smeets, V. P. Dravid, X. Hu, *Proc. Natl. Acad. Sci. USA* **2022**, *119*, 1.
[27] B. Pokroy, A. N. Fitch, E. Zolotoyabko, *Adv. Mater.* **2006**, *18*, 2363.
[28] B. Pokroy, M. Kapon, F. Marin, N. Adir, E. Zolotoyabko, *Proc. Natl. Acad. Sci. USA* **2007**, *104*, 7337.
[29] B. Pokroy, A. N. Fitch, F. Marin, M. Kapon, N. Adir, E. Zolotoyabko, *J. Struct. Biol.* **2006**, *155*, 96.
[30] A. Ulvestad, A. Singer, J. N. Clark, H. M. Cho, J. W. Kim, R. Harder, J. Maser, Y. S. Meng, O. G. Shpyrko, *Science* **2015**, *348*, 1344.
[31] A. R. Passos, A. Rochet, L. M. Manente, A. F. Suzana, R. Harder, W. Cha, F. Meneau, *Nat. Commun.* **2020**, *11*, 4733.
[32] N. Spanos, P. G. Koutsoukos, *J. Phys. Chem. B* **1998**, *102*, 6679.
[33] D. Li, M. H. Nielsen, J. R. I. Lee, C. Frandsen, J. F. Banfield, J. J. De Yoreo, *Science* **2012**, *336*, 1014.
[34] A. Putnis, *J. Petrol.* **2021**, *62*, 1.
[35] L. Jonas, T. John, H. E. King, T. Geisler, A. Putnis, *Earth Planet. Sci. Lett.* **2014**, *386*, 64.
[36] J. R. Fienup, *Appl. Opt.* **1982**, *21*, 2758.
[37] C. C. Chen, J. Miao, C. W. Wang, T. K. Lee, *Phys. Rev. B: Condens. Matter Mater. Phys.* **2007**, *76*, 064113.
[38] S. Marchesini, H. He, N. Chapman, P. Hau-Riege, A. Noy, R. Howells, U. Weierstall, H. X.-R. Spence, *Phys. Rev. B: Condens. Matter Mater. Phys.* **2003**, *68*, 140101.

[39] J. Ahrens, B. Geveci, C. Law, *The Visualization Handbook*, Elsevier, Oxford **2005**, https://citeseerx.ist.psu.edu/document?repid=rep1amp;type=pdfamp;doi=37289ca24fde4c63281c061815d625c7acee1e6a#page=736.

[40] C. M. Bethke, S. Yeakel, in *The Geochemist's Workbench Release 10.0: GWB Essentials Guide*, Aqueous Solutions, LLC, Champaign, IL **2015**, p. 116.

[41] D. Langmuir, *Aqueous Environmental Geochemistry*, Prentice-Hall, Upper Saddle River, NJ **1997**.